Synergistically improved hydrogen evolution by interface engineering of monodispersed $Co_{5.47}N/CoMoO_x$ hybrid particles on carbon cloth with rich oxygen vacancies

Zhiyang Huang [a], Zhengqi Liu [a], Miao Liao [a], Lixia Wang [a], Zuyang Luo [a], Tayirjan Taylor Isimjan [b], Xiulin Yang [a],[*]

[a] Guangxi Key Laboratory of Low Carbon Energy Materials, School of Chemistry and Pharmaceutical Sciences, Guangxi Normal University, Guilin 541004, China
[b] Saudi Arabia Basic Industries Corporation (SABIC) at King Abdullah University of Science and Technology (KAUST), Thuwal 23955-6900, Saudi Arabia

ARTICLE INFO

ABSTRACT

Designing the basic steps of water dissociation and hydrogen desorption rationally is essential to comprehend the role of oxygen vacancies in hydrogen evolution reaction (HER). This study uses interface and defect engineering to produce monodispersed $Co_{5.47}N/CoMoO_x$ hybrid particles on carbon cloth with abundant oxygen vacancies. The optimized $Co_{5.47}N/CoMoO_x$ catalyst shows a low overpotential of 36 mV at 10 mA cm^{-2}, similar to commercial Pt/C. Additionally, the overall water splitting with $Co_{5.47}N/CoMoO_x$ as cathode has a cell voltage of 1.74 V at 100 mA cm^{-2}, better than $Pt/C^{(-)} || RuO_2^{(+)}$, and operates stably for 50 h at 100 mA cm^{-2} without degradation, making it a promising electrocatalyst for industrial use. Experiment and DFT calculations demonstrate that strong electronic interaction between different components and rich oxygen vacancies enhance the catalyst's electrical conductivity and water dissociation. As a result, the hydrogen adsorption free energy (ΔG_{H^*}, −0.06 eV) is nearly equal to the ideal adsorption energy (0 eV), demonstrating faster hydrogen absorption/desorption kinetics for $Co_{5.47}N/CoMoO_x$, thus improving its HER performance.

1. Introduction

Compared to traditional fossil fuels (oil, coal, natural gas, etc.), hydrogen (H_2), with high-energy density, carbon-free, and sustainable merits, is regarded as the most potential new energy in the 21st century [1,2]. For the conventional hydrogen production method such as methane reforming, electrochemical water splitting is an ideal method so far [3]. Nevertheless, the HER overpotential increases significantly in alkaline media, resulting in higher electric power consumption [4]. Although Pt-based electrocatalysts show optimal HER performance, the high cost and scarcity can seriously hamper its widespread utilization [5,6]. Therefore, it's crucial to design and create low-cost and efficient non-noble metal catalysts as a replacement for expensive noble metal catalysts.

Recently, numerous transition metal compounds have shown excellent HER performance in electrochemical water splitting, such as sulfides [7], oxides [8], phosphides [9], carbides [10] and nitrides [11] and so on. Transition metal nitrides (TMNs) are considered promising materials for superseding platinum-based electrocatalysts because of their

outstanding catalytic activity, excellent electrical conductivity, and corrosion resistance [12]. In contrast, the metal center's intense hydrogen bonding energy (HBE) results in the HER performance of TMNs being considerably lower than that of commercial Pt/C [13]. Moreover, the sluggish water adsorption/dissociation steps cause the tardy kinetics of alkaline HER. Simultaneously, the mechanism of alkaline HER can be segmented into the water dissociation (Volmer step: $H_2O + e^- \rightarrow H_{ad} + OH^-$), as well as the associative desorption of molecular H_2 (Heyrovsky step: $H_{ad} + H_2O + e^- \rightarrow H_2 + OH^-$ or Tafel step: $2H_{ad} \rightarrow H_2$). Consequently, additional species can be introduced to lower the water adsorption/dissociation energy barrier, thereby enhancing the alkaline HER activity of TMNs [13]. Interestingly, the high-valent metal ions in the metal oxides are advantageous for breaking the O-H bond of adsorbed water [14]. For instance, Hu et al. demonstrated that the synergistic impact of $Co_2Mo_3O_8$ and Co_2N made the $Co_2N/Co_2Mo_3O_8$ heterojunction exhibit remarkable HER activity [15]. Yao et al. confirmed that the electronic interaction between CoO and Co_4N could stimulate the H_2O adsorption and optimize the HBE, thereby enhancing the catalytic activity of Co_4N [16]. Furthermore, oxygen vacancies

---

* Corresponding author.
E-mail address: xlyang@gxnu.edu.cn (X. Yang).
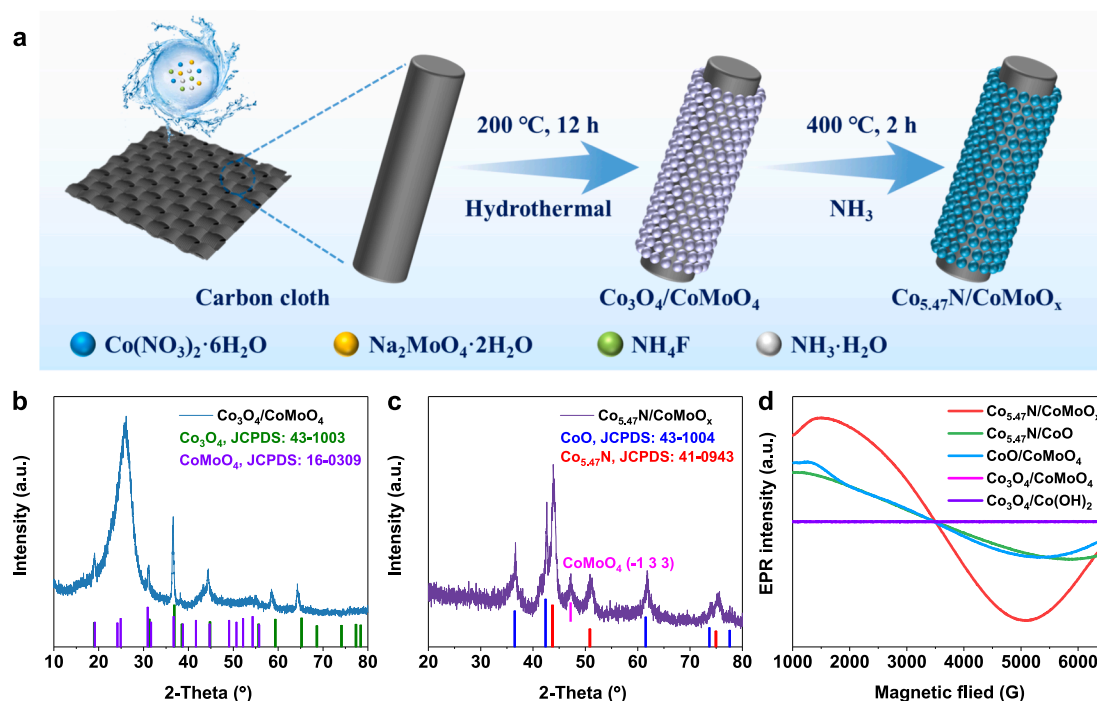
Fig. 1. (a) Schematic illustration for the synthetic strategy of $Co_{5.47}N/CoMoO_x$. XRD patterns of (b) $Co_3O_4/CoMoO_4$, and (c) $Co_{5.47}N/CoMoO_x$. (d) EPR spectra of $Co_{5.47}N/CoMoO_x$, $Co_{5.47}N/CoO$, $CoO/CoMoO_4$, $Co_3O_4/CoMoO_4$ and $Co_3O_4/Co(OH)_2$.

facilitate water dissociation, accelerate the charge transfer and improve electrical conductivity [17]. From this, heterogeneous materials comprised of different types and properties of materials provide many degrees of freedom for catalyst design. Therefore, it is recommended to create heterojunction catalysts with oxygen vacancies through interface engineering and introduction of defects.

This study aims to synthesize uniformly dispersed particles comprising $Co_{5.47}N$, CoO, and $CoMoO_4$ ($Co_{5.47}N/CoMoO_x$) on carbon cloth through hydrothermal and gas-phase nitridation treatment in sequence. Experimental and theoretical analyses will be conducted to evaluate the impact of the intense electron interaction and abundant oxygen vacancies of the $Co_{5.47}N/CoMoO_x$ hybrid catalyst on reducing water-dissociation energy and accelerating the HER process. The study will also investigate the effect of Mo^{4+} and Mo^{5+} in $Co_{5.47}N/CoMoO_x$ on boosting hydrogen release. Finally, the industrial implications of the cell voltage of $Co_{5.47}N/CoMoO_x^{(-)} || RuO_2^{(+)}$ will be examined in comparison to commercial $Pt/C^{(-)} || RuO_2^{(+)}$ at 100 mA cm^{-2}.

2. Experimental section

2.1. Synthesis of $Co_3O_4/CoMoO_4$ particles on CC

All chemicals used in this work are of analytical grade. Initially, 1.5 mmol $Na_2MoO_4·2H_2O$ and 8 mmol NH_4F were dissolved in 25 mL deionized (DI) water. After stirring for 10 min, 10 mL $NH_3·H_2O$ was added into the above solution with stirring (solution A). In addition, 1.5 mmol $Co(NO_3)_2·6H_2O$ was dissolved in 25 mL DI water through sonication (solution B). After that, solution B was added to solution A with stirring. Meanwhile, a piece of CC (1.5 cm × 3 cm) was cleaned ultrasonically in 0.5 M H_2SO_4, DI water and ethanol. Subsequently, the mixed solution and pretreated CC were transferred into a Teflon-line stainless steel autoclave and heated at 200 °C for 12 h. After cooling, the produced CC was fetched, washed with DI water and dried. The product was named $Co_3O_4/CoMoO_4$. For comparison, the Mo doping level was adjusted by altering the Co/Mo molar ratio (3:0, 2:1, 1:2) during the synthesis process. The synthesized samples were named $Co_3O_4/Co(OH)_2$, $Co_3O_4/CoMoO_4$-2, and $Co_3O_4/CoMoO_4$-0.5. The total amount of

Co/Mo substance was 3 mmol.

2.2. Synthesis of $Co_{5.47}N/CoMoO_x$ particles on CC

The $Co_3O_4/CoMoO_4$ was annealed at different temperatures (300, 400 and 500 °C) for 2 h under a flowing NH_3 atmosphere with a heating rate of 5 °C min^{-1}. The samples obtained were Co_xO_y/MoO_3-300, $Co_{5.47}N/CoMoO_x$-400 and $Co_{5.47}N/CoMoO_x$-500, respectively. Unless otherwise specified, the $Co_{5.47}N/CoMoO_x$ was obtained at 400 °C. And the mass loading of $Co_{5.47}N/CoMoO_x$ on CC was 0.75 mg cm^{-2}. The $CoO/CoMoO_4$ was fabricated with a similar procedure by utilizing a 5% H_2/Ar atmosphere as a control. And the preparation of $Co_{5.47}N/CoO$ on CC was analogous to that of $Co_{5.47}N/CoMoO_x$, except that $Co_3O_4/CoMoO_4$ was substituted by $Co_3O_4/Co(OH)_2$.

RuO_2 and Pt/C powders were cast onto the CC surface with a loading of 0.75 mg cm^{-2} as described in Supporting Information. The corresponding XRD pattern was indexed to RuO_2 (JCPDS: 40-1290), confirming the successful preparation of RuO_2 (Fig. S2).

3. Results and discussion

3.1. Synthesis and structural analysis

The synthetic process for $Co_{5.47}N/CoMoO_x$ on CC is illustrated in Fig. 1a. Firstly, $Co_3O_4/CoMoO_4$ particles were grown in situ on CC via a hydrothermal method. Subsequently, the $Co_3O_4/CoMoO_4$ was converted into $Co_{5.47}N/CoMoO_x$ using a controllable thermal treatment under the NH_3 atmosphere.

X-ray powder diffraction (XRD) elucidated the crystalline structure of as-prepared catalysts. Fig. 1b showed that the XRD patterns of $Co_3O_4/CoMoO_4$ on CC were composed of Co_3O_4 (JCPDS: 43-1003) [18] and $CoMoO_4$ (JCPDS: 16-0309) [19]. The diffraction peak at approximately 25.8° was assigned to the carbon cloth substrate [20]. The powder was scraped from the CC substrate for further XRD investigation because of the low mass loading of $Co_{5.47}N/CoMoO_x$ on CC. As depicted in Fig. 1c, the diffraction peaks of $Co_{5.47}N/CoMoO_x$ were indexed to $Co_{5.47}N$ (JCPDS: 41-0943) [21], CoO (JCPDS: 43-1004) [22] and $CoMoO_4$
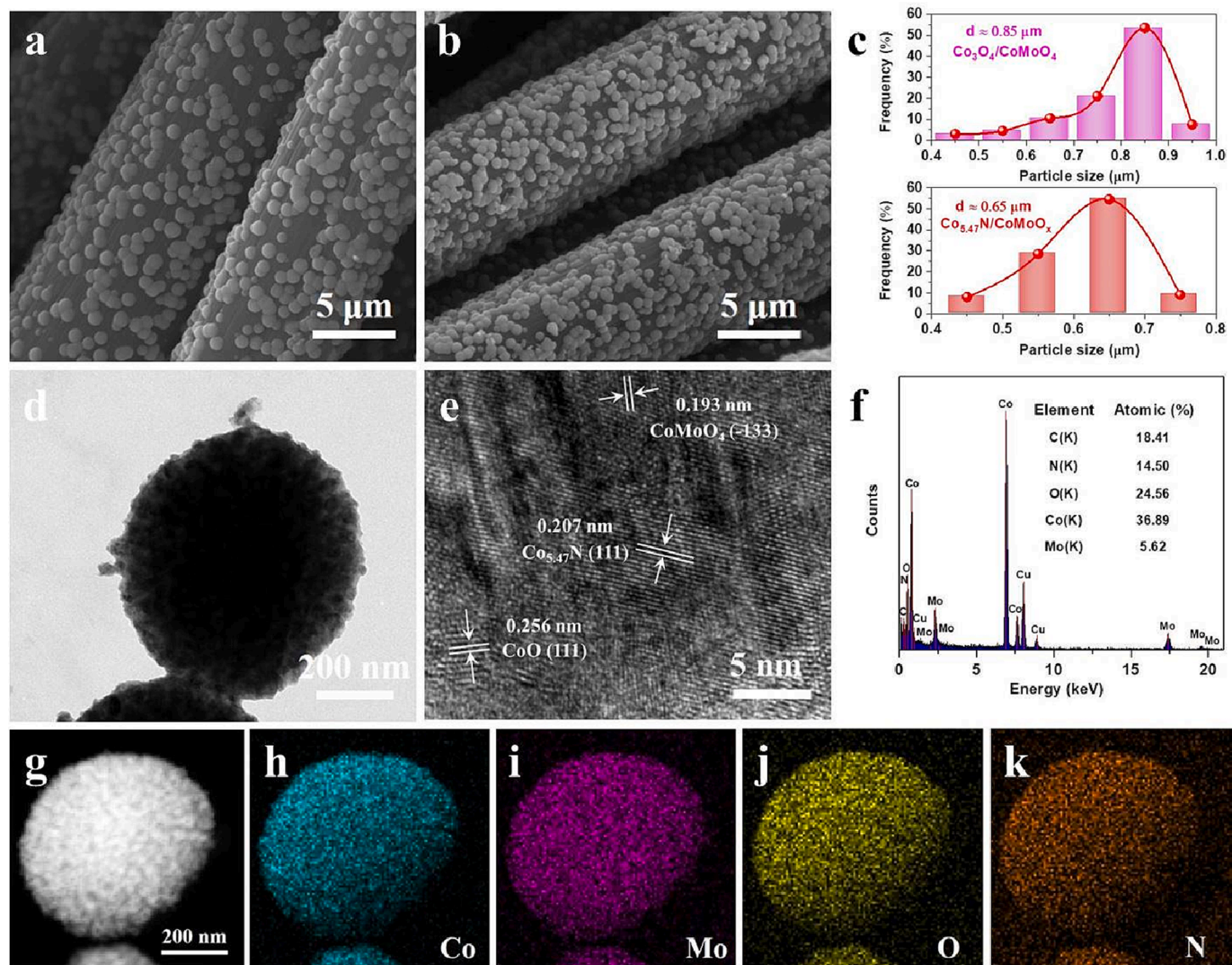
Fig. 2. SEM images of (a) $Co_3O_4/CoMoO_4$ and (b) $Co_{5.47}N/CoMoO_x$. (c) Particle diameter histograms of $Co_3O_4/CoMoO_4$ and $Co_{5.47}N/CoMoO_x$. (d) TEM, (e) HR-TEM images and (f) EDX pattern of $Co_{5.47}N/CoMoO_x$. (g-k) HAADF-STEM images of $Co_{5.47}N/CoMoO_x$ and elemental mappings of Co, Mo, O, and N.

(JCPDS: 25-1434) [23], respectively. After annealing at 400 ℃ for 2 h at 5% H_2/Ar atmosphere, the $Co_3O_4/CoMoO_4$ was transformed into CoO and $CoMoO_4$ (Fig. S3a). In addition, $Co_3O_4/Co(OH)_2$ was found to contain Co_3O_4 and $Co(OH)_2$ (JCPDS: 51-1731) (Fig. S3b) [24]. The $Co_{5.47}N/CoO$ was comprised of $Co_{5.47}N$ and CoO (Fig. S3c). It was worth noting that the crystal structures of $Co_3O_4/CoMoO_4$-x (x = 2, 1 and 0.5) didn't change during the Mo doping process. Specifically, their diffraction peaks had a little negative shift compared with those of $Co_3O_4/Co(OH)_2$, which could be ascribed to the change of lattice parameters of the cubic Co_3O_4 induced by Mo doping (Fig. S4) [25,26]. During ammonia pyrolysis, the calcination temperature significantly influenced the crystal structure of catalysts. As depicted in Fig. S5, Co_xO_y/MoO_3-300 was composed of CoO, Co_3O_4 and a small amount of MoO_3 (JCPDS: 35-0609). At 400 ℃, the XRD signals of Co_3O_4 disappeared, while $Co_{5.47}N$ and $CoMoO_4$ phases began to appear. Interestingly, while the crystal structures of the samples at 400 and 500 ℃ were similar, the XRD signals of $Co_{5.47}N$ were amplified. In contrast, CoO and $CoMoO_4$ were significantly attenuated at 500 ℃, indicating that higher temperature was favorable to the formation of $Co_{5.47}N$. Therefore, $Co_{5.47}N/CoO/CoMoO_4$ obtained at 400 ℃ may be one of the critical reasons for improving its electrochemical performance. In addition, electron paramagnetic resonance (EPR) showed that the hybrid catalyst appeared an obvious EPR signal of unpaired electron at g = 2.000, indicating that the hybrid

catalyst had rich oxygen vacancies (Fig. 1d) [27]. Oxygen vacancies play a crucial role in modifying the electronic structures and thereby enhancing the electrical conductivity, as reported in various literature sources [28–30].

Scanning electron microscopy (SEM) was used to reveal various catalysts' morphology. As seen in Fig. 2a, $Co_3O_4/CoMoO_4$ exhibited particulate characteristics with good dispersion. After annealing treatment in NH_3, the particulate morphology could be well preserved (Fig. 2b), and the average particle size decreased from 0.85 μm to 0.65 μm (Fig. 2c). $Co_3O_4/Co(OH)_2$ presented a cubic structure, which demonstrated that the morphology of catalysts was associated with the introduction of Mo (Fig. S6a). Although $Co_{5.47}N/CoO$ inherited the cubic structure, its surface became rough (Fig. S6b). Besides, the SEM images of $Co_3O_4/CoMoO_4$-x (x = 2, 1 and 0.5) were seen in Fig. S7. $Co_3O_4/CoMoO_4$-2 displayed large particles with serious conglutination, while $Co_3O_4/CoMoO_4$-0.5 showed small particles. The results demonstrated that adding Mo could improve the particulate morphology of catalysts, and the particle size decreased further with the increase of Mo content. Therefore, an appropriate Co/Mo molar ratio was favourable for forming uniformly dispersed particles, exposing abundant active sites and accelerating the mass transfer rate. As depicted in Fig. S8, the morphology of catalysts was also related to the annealing temperature. Compared with Co_xO_y/MoO_3-300 and $Co_{5.47}N/CoMoO_x$-400, the
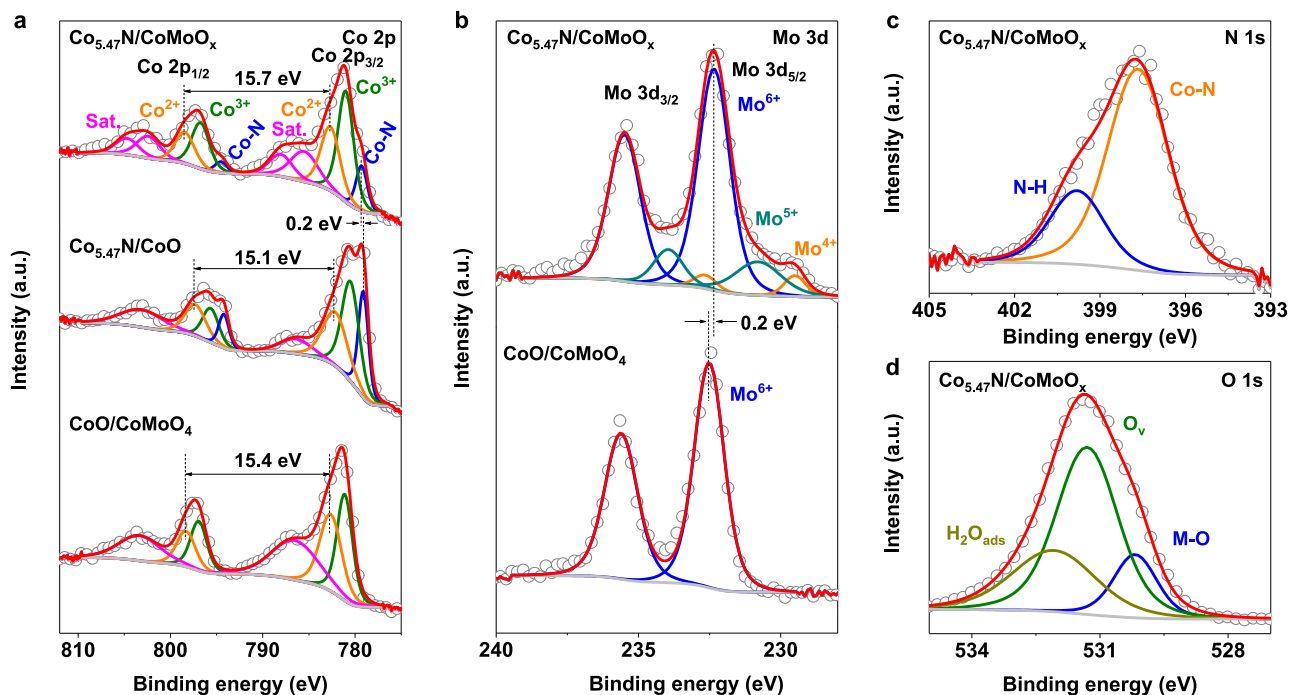
Fig. 3. High-resolution XPS spectra of (a) Co 2p and (b) Mo 3d of $Co_{5.47}N/CoMoO_x$, $Co_{5.47}N/CoO$ and $CoO/CoMoO_4$, respectively. (c) N 1s and (d) O 1s of $Co_{5.47}N/CoMoO_x$.

particles of $Co_{5.47}N/CoMoO_x$-500 were significantly agglomerated, manifesting that increasing the annealing temperature will lead to particle aggregation. Transmission electron microscopy (TEM) was performed to investigate the microstructure of $Co_{5.47}N/CoMoO_x$. The TEM image (Fig. 2d) of $Co_{5.47}N/CoMoO_x$ demonstrated a mono-dispersed particle morphology consistent with the SEM image. Additionally, the high-resolution TEM (HR-TEM) image (Fig. 2e) elucidated lattice plane spacing of 0.256 nm, 0.207 nm and 0.193 nm, matching with the plane of CoO (1 1 1), $Co_{5.47}N$ (1 1 1) and $CoMoO_4$ (−1 3 3), respectively. The energy dispersive X-ray (EDX) spectroscopy displayed the Co, Mo, O and N signals in $Co_{5.47}N/CoMoO_x$ (Fig. 2f). As depicted in Fig. 2g-k, the particulate structure was further confirmed by high-angle annular dark-field scanning TEM (HAADF-STEM), as well element mappings verified that Co, Mo, O and N were evenly distributed in $Co_{5.47}N/CoMoO_x$.

Moreover, the surface area and pore size of $Co_{5.47}N/CoMoO_x$ particles were calculated using an N_2 adsorption–desorption isotherm. As depicted in Fig. S9, the isotherm was of type IV with a clear H_3 type hysteresis loop, indicating the presence of mesoporous structure [31,32]. The Brunauer-Emmett-Teller (BET) analysis showed that the $Co_{5.47}N/CoMoO_x$ has a specific surface area of 45.2 m^2 g^{-1} and an average pore diameter of 29.2 nm, contributing to its catalytic activity through abundant active sites and efficient mass transfer ability [33].

X-ray photoelectron spectroscopy (XPS) was deployed to recognize the element composition and surface chemical valence states of catalysts. The XPS survey spectra could obviously illustrate in possession of Co, Mo, N, O and C elements in $Co_{5.47}N/CoMoO_x$ (Fig. S10a). The high-resolution C 1s spectrum of $Co_{5.47}N/CoMoO_x$ was deconvoluted into C-C (284.8 eV) and C-O (285.8 eV) (Fig. S10b) [34]. As presented in Fig. 3a, the Co 2p XPS core-level spectrum of $Co_{5.47}N/CoMoO_x$ revealed that the peaks occurring at 781.0 eV and 782.7 eV corresponded to the Co^{3+} $2p_{3/2}$ and Co^{2+} $2p_{3/2}$, respectively [35]. Additionally, the peaks at 779.3 eV and 794.5 eV for Co $2p_{3/2}$ and Co $2p_{1/2}$ in $Co_{5.47}N/CoMoO_x$ indicated the presence of Co-N [36], implying the successful synthesis of Co nitrides. Notably, the doublet separation energy of $Co_{5.47}N/CoMoO_x$ (15.7 eV) was higher than that of $Co_{5.47}N/CoO$ (15.1 eV) and $CoO/CoMoO_4$ (15.4 eV). Consequently, the enlarged splitting value demonstrated

intense electron interaction in $Co_{5.47}N/CoMoO_x$ [37]. As viewed in Fig. 3b, the Mo 3d spectrum of $Co_{5.47}N/CoMoO_x$ demonstrated three Mo species: Mo^{4+} (at 229.5 and 232.7 eV), Mo^{5+} (at 230.8 and 233.9 eV), and Mo^{6+} (at 232.3 and 235.5 eV) [14,35]. Due to the reduction of NH_3, the high-valence state of Mo^{6+} is reduced to the low-valence state of Mo^{4+} and Mo^{5+}, resulting in the loss of lattice oxygen and the formation of oxygen vacancies. According to the XPS peak area of Mo 3d, the cations of Mo^{6+}, Mo^{5+} and Mo^{4+} account for 77.8 %, 17.2 % and 5 % of the total Mo states in $Co_{5.47}N/CoMoO_x$, respectively. Therefore, the average oxidation state of Mo is 5.73 by XPS sub-peak area, which is the mixed-valence state arising from the oxygen vacancies [38]. In addition, the multiple valence states and metallic properties of $Co_{5.47}N/CoMoO_x$ could improve its electrocatalytic activity [39]. Surprisingly, the Co-N peak in $Co_{5.47}N/CoMoO_x$ shifted to higher binding energy (0.2 eV) in comparison with that of $Co_{5.47}N/CoO$. Meanwhile, the binding energy of Mo^{6+} was reduced by 0.2 eV relative to $CoO/CoMoO_4$. The shift of binding energy indicated a strong electron interaction between Co species and Mo species at the $Co_{5.47}N/CoMoO_x$ [40]. The N 1s spectrum (Fig. 3c) indicated a predominant Co-N signal (397.7 eV), further corroborating the formation of Co nitrides [15,41]. The additional peak at 399.8 eV could derive from the N-H surface terminal group after NH_3 treatment.[42,43] For the high-resolution spectrum of O 1s for $Co_{5.47}N/CoMoO_x$ (Fig. 3d), the peaks located at 530.2, 531.3, and 532.1 eV were ascribed to metal–oxygen (M−O) bonds, oxygen vacancies (O_v), and adsorbed H_2O molecules (H_2O_{ads}), respectively [44]. Therefore, both XPS and EPR results validated that $Co_{5.47}N/CoMoO_x$ possessed abundant oxygen vacancies, which could provide active sites and facilitate electron transfer, thereby improving catalytic activity [45,46].

3.2. HER activities in alkaline medium

The HER performance of diverse catalysts was measured by linear sweep voltammetry (LSV) employing a typical three-electrode electrochemical system in a 1.0 M KOH solution. All potentials were iR compensated and calibrated to the reversible hydrogen electrode (RHE) (Fig. S1). The Figs. S11–S14 and Tables S1 and S2 showed the electrochemical performance of the optimized Co/Mo doping level and

3.2. HER activities in alkaline medium
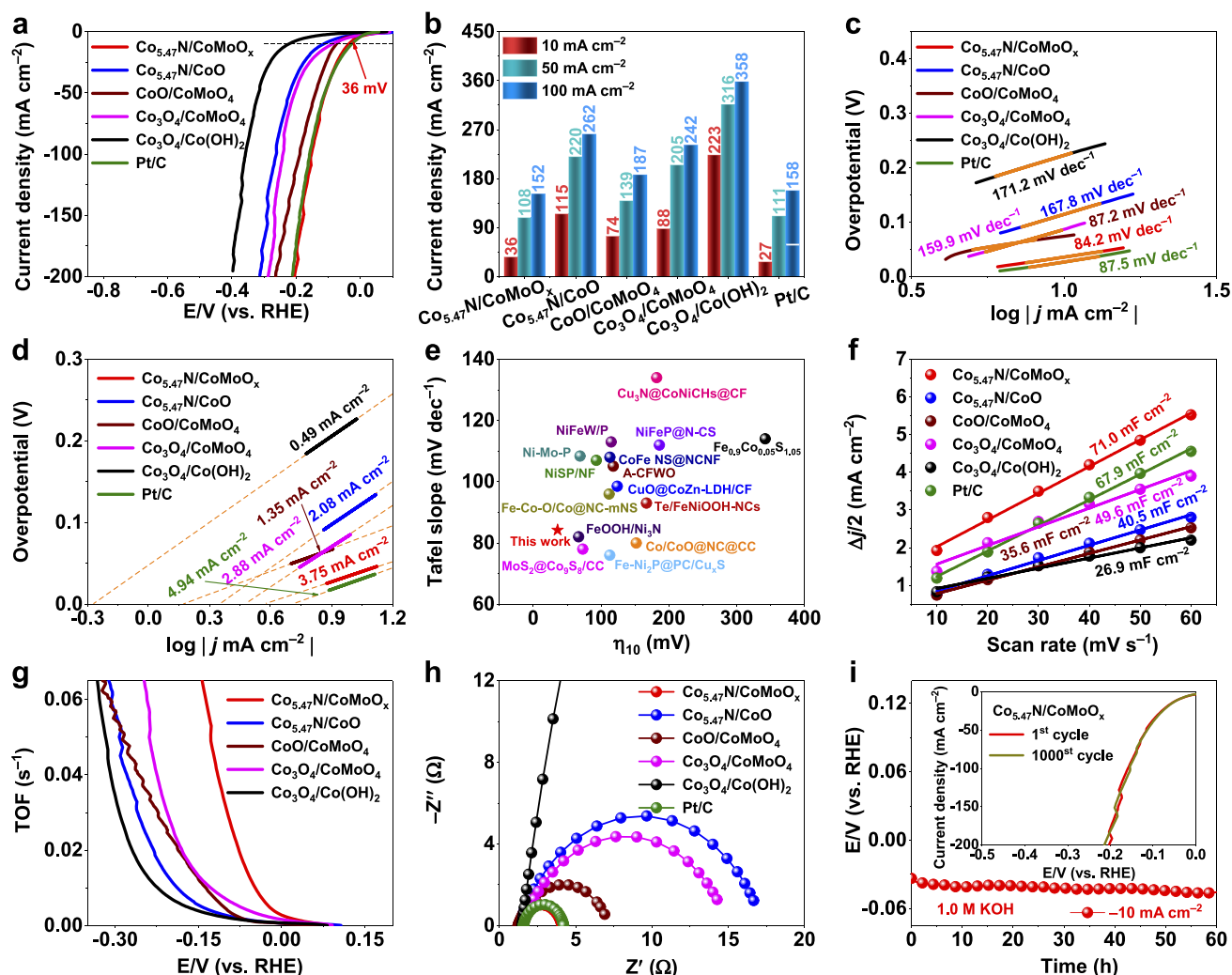
Fig. 4. Electrocatalytic HER tests in 1.0 M KOH electrolyte using a three-electrode system for $Co_{5.47}N/CoMoO_x$, $Co_{5.47}N/CoO$, $CoO/CoMoO_4$, $Co_3O_4/CoMoO_4$, $Co_3O_4/Co(OH)_2$ and Pt/C. (a) LSV polarization curves, (b) overpotentials at 10, 50 and 100 mA cm^{-2}, (c) Tafel slopes, (d) exchange current density (j_0), (e) comparison the overpotential at -10 mA cm^{-2} and Tafel slope with previously reported catalysts, (f) double-layer capacitance (C_{dl}) plots, (g) turnover frequency (TOF) value, (h) Nyquist plots and (i) chronopotentiometry of $Co_{5.47}N/CoMoO_x$ at 10 mA cm^{-2} (inset: polarization curves of $Co_{5.47}N/CoMoO_x$ before and after 1000 cycles).

nitriding temperature, respectively. The results indicated that the optimum catalyst was synthesized when the molar ratio of Co/Mo was 1:1 and the nitriding temperature was 400 ℃. Therefore, the $Co_{5.47}N/CoMoO_x$ discussed below was obtained under the optimum synthesis conditions.

As described in Fig. 4a, $Co_{5.47}N/CoMoO_x$ performed significant HER activity ($\eta_{10} = 36$ mV) comparable to commercial Pt/C ($\eta_{10} = 27$ mV), and surpassed all other controls [$Co_{5.47}N/CoO$ ($\eta_{10} = 115$ mV), CoO/ $CoMoO_4$ ($\eta_{10} = 74$ mV), $Co_3O_4/CoMoO_4$ ($\eta_{10} = 88$ mV), and Co_3O_4/Co $(OH)_2$ ($\eta_{10} = 223$ mV)]. At high current densities, the polarization curves become unstable due to the impact of the rapidly produced hydrogen bubbles on the connection between the electrode surface and the electrolyte. In particular, $Co_{5.47}N/CoMoO_x$ could deliver ultralow overpotentials of 108 and 152 mV at 50 and 100 mA cm^{-2}, respectively (Fig. 4b). The Tafel slopes were calculated to evaluate the reaction kinetics (Fig. 4c). The $Co_{5.47}N/CoMoO_x$ exhibited a lower Tafel slope (84.2 mV dec^{-1}) than that of commercial Pt/C (87.5 mV dec^{-1}), $Co_{5.47}N/CoO$ (167.8 mV dec^{-1}), $CoO/CoMoO_4$ (87.2 mV dec^{-1}), $Co_3O_4/$ $CoMoO_4$ (159.9 mV dec^{-1}), and $Co_3O_4/Co(OH)_2$ (171.2 mV dec^{-1}),

attesting the favourable reaction kinetics of $Co_{5.47}N/CoMoO_x$. Besides, $Co_{5.47}N/CoMoO_x$ underwent the Volmer-Heyrovsky mechanism [47,48]. The exchange current density (j_0) obtained by extrapolating the Tafel slope reflected the intrinsic HER catalytic activity (Fig. 4d). The j_0 value of $Co_{5.47}N/CoMoO_x$ (3.75 mA cm^{-2}) was much higher than all other control samples except Pt/C, confirming the high intrinsic HER activity of $Co_{5.47}N/CoMoO_x$. In addition, the exceptional HER performance of $Co_{5.47}N/CoMoO_x$ also surpassed most of the previously reported catalysts (Fig. 4e and Table S3).

To further identify the source of decent HER activity, the electrochemical active surface area (ECSA) of catalysts was estimated by measuring the electrochemical double-layer capacitance (C_{dl}) (Fig. 4f and Fig. S15). The C_{dl} of $Co_{5.47}N/CoMoO_x$ was 71.0 mF cm^{-2}, higher than that of $Co_{5.47}N/CoO$ (40.5 mF cm^{-2}), $CoO/CoMoO_4$ (35.6 mF cm^{-2}), $Co_3O_4/CoMoO_4$ (49.6 mF cm^{-2}), $Co_3O_4/Co(OH)_2$ (26.9 mF cm^{-2}) and Pt/C (67.9 mF cm^{-2}). The $Co_{5.47}N/CoMoO_x$ had a maximum ECSA of 1775.0 cm^2 (Fig. S16), which illustrated that $Co_{5.47}N/CoMoO_x$ was capable of exposing more active sites for HER [49]. Moreover, the intrinsic catalytic activity was evaluated using turnover frequency (TOF)
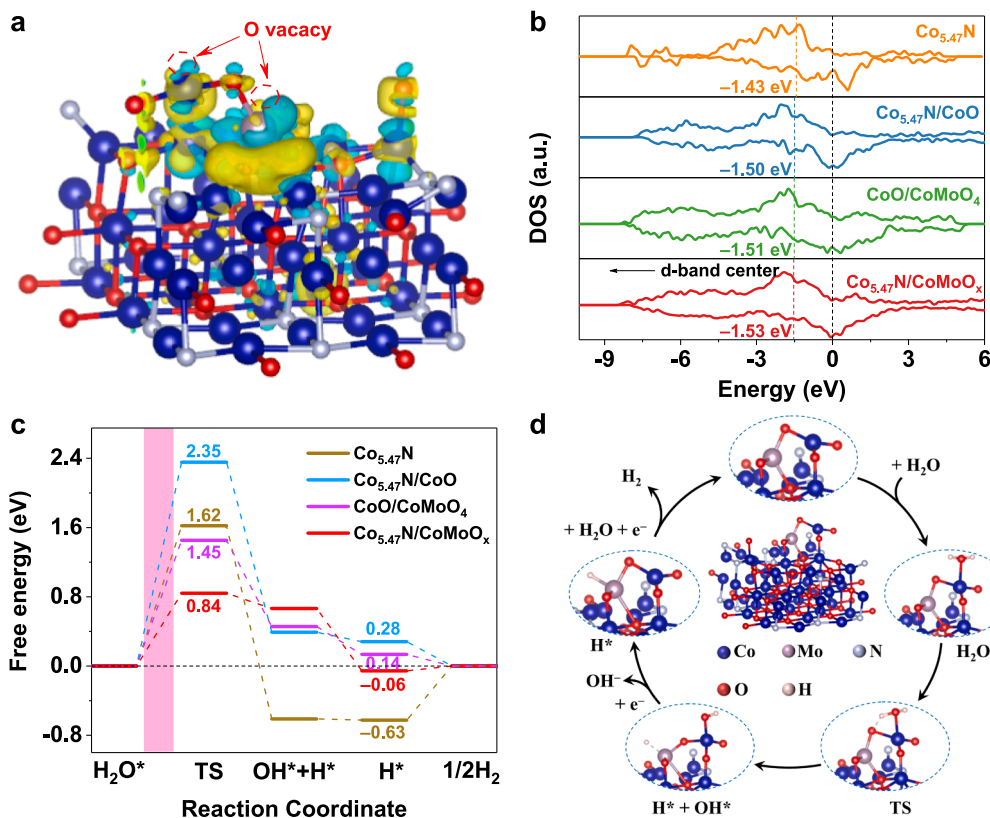
Fig. 5. Density functional theory (DFT) calculations. (a) The charge density difference of $Co_{5.47}N/CoMoO_x$ model. The cyan and yellow region represent the depletion of electrons and the accumulation of electrons, respectively. (b) The density of states (DOS) of $Co_{5.47}N$, $Co_{5.47}N/CoO$, $CoO/CoMoO_4$ and $Co_{5.47}N/CoMoO_x$ systems. (c) Gibbs free energy diagrams for HER on $Co_{5.47}N$, $Co_{5.47}N/CoO$, $CoO/CoMoO_4$ and $Co_{5.47}N/CoMoO_x$. (d) HER mechanism illustration of $Co_{5.47}N/CoMoO_x$. (For interpretation of the references to colour in this figure legend, the reader is referred to the web version of this article.)

calculated from the ICP results (Table S4) [50]. As seen in Fig. 4g, the TOF value of $Co_{5.47}N/CoMoO_x$ (0.0315 H_2 s^{-1}) at an overpotential of 100 mV is higher than those of $Co_3O_4/CoMoO_4$ (0.00714 H_2 s^{-1}), $Co_{5.47}N/CoO$ (0.00271 H_2 s^{-1}), $CoO/CoMoO_4$ (0.00467 H_2 s^{-1}), and $Co_3O_4/Co(OH)_2$ (0.00215 H_2 s^{-1}), affirming the outstanding inherent activity of $Co_{5.47}N/CoMoO_x$. The Nyquist plots (Fig. 4h) showed that $Co_{5.47}N/CoMoO_x$ had a lower charge transfer resistance, indicating higher electrical conductivity and more efficient charge transfer [51]. This superior electrical conductivity can be attributed to the presence of abundant oxygen vacancies. The long-term stability of $Co_{5.47}N/CoMoO_x$ was investigated as well (Fig. 4i). $Co_{5.47}N/CoMoO_x$ slightly decreased when subjected to chronopotentiometry at a current density of 10 mA cm^{-2} for 60 h. In addition, the HER performance of $Co_{5.47}N/CoMoO_x$ remained highly after 1000 cycles of CV scans, further demonstrating superior stability. The morphology and chemical structure of the catalyst were characterized using SEM and XPS. Results showed that the catalyst's morphological structure remained intact after a long-term stability test, and XPS spectra indicated that the $Co_{5.47}N/CoMoO_x$ maintained its original chemical state, confirming its good stability for HER (Figs. S17 and S18) [52].

3.3. DFT calculations

Density functional theory (DFT) calculations were conducted further to understand the superior HER performance of $Co_{5.47}N/CoMoO_x$. The optimized structure models of $Co_{5.47}N$, $Co_{5.47}N/CoO$, $CoO/CoMoO_4$ and $Co_{5.47}N/CoMoO_x$ were shown in Fig. S19. The charge density analysis indicated visible charge accumulation at the interface, effectively confirming a strong electron interaction between CoO, $CoMoO_4$ and $Co_{5.47}N$ (Fig. 5a). Moreover, there are oxygen vacancies in $CoMoO_4$ of $Co_{5.47}N/CoMoO_x$. Additionally, the density of states (DOS) demonstrated that the d-band center (ε_d) of $Co_{5.47}N/CoMoO_x$ was at −1.53 eV away from the Fermi level compared with those of $Co_{5.47}N$ (−1.43 eV), $Co_{5.47}N/CoO$ (−1.50 eV) and $CoO/CoMoO_4$ (−1.51 eV) (Fig. 5b). The lower-lying d-

band center would lead to lower antibonding energy states and weakened interactions between adsorbed H and the catalyst, thereby expediting H desorption and HER kinetics [53,54]. To intuitively comprehend the HER kinetics, the reaction barriers for elementary steps were calculated, including the barrier of the H_2O dissociation process and the hydrogen desorption energy (Fig. 5c). Generally, the Volmer step (water dissociation) is regarded as the rate-determining step for alkaline HER [55]. The water dissociation energy barrier of $Co_{5.47}N/CoMoO_x$ was 0.84 eV, lower than that of $Co_{5.47}N$ (1.62 eV), $Co_{5.47}N/CoO$ (2.35 eV) and $CoO/CoMoO_4$ (1.45 eV), which accelerated the dissociation of water into OH* and H*, thereby achieving rapid proton supply and promoting the HER kinetics [53,56]. The desirable energy barrier of $Co_{5.47}N/CoMoO_x$ may be ascribed to the existence of oxygen vacancies, which are beneficial to facilitate the dissociation of water [14,57]. Moreover, the free energy of hydrogen adsorption/desorption (ΔG_{H*}) is another critical parameter that evaluates the HER activity. Generally, the ΔG_{H*} value of a suitable HER catalyst needs to be close to zero ($\Delta G_{H*} \approx 0$ eV) [53]. $Co_{5.47}N/CoMoO_x$ possessed the more favourable ΔG_{H*} value of − 0.06 eV, extremely close to the ideal adsorption energy (0 eV), which testified to the faster hydrogen absorption/desorption kinetics of $Co_{5.47}N/CoMoO_x$. Based on experimental and theoretical results, the alkaline HER mechanism of the $Co_{5.47}N/CoMoO_x$ was proposed in Fig. 5d. Firstly, the H_2O molecule was adsorbed on the Co atoms of $CoMoO_4$. Subsequently, the OH$^-$ and H* intermediates can be produced by the activation and dissociation of H_2O. The high-valence state of Mo^{6+} in $CoMoO_4$ is favorable for weakening the O-H bond of adsorbed water, thus facilitating water dissociation [14,58]. Ultimately, H* adsorption and desorption occurred on the Mo atoms of $CoMoO_4$ since the Mo^{4+} and Mo^{5+} can boost the desorption of the generated H_2 [59].

3.4. Overall water splitting analysis

Motivated by the remarkable HER performance of $Co_{5.47}N/CoMoO_x$,
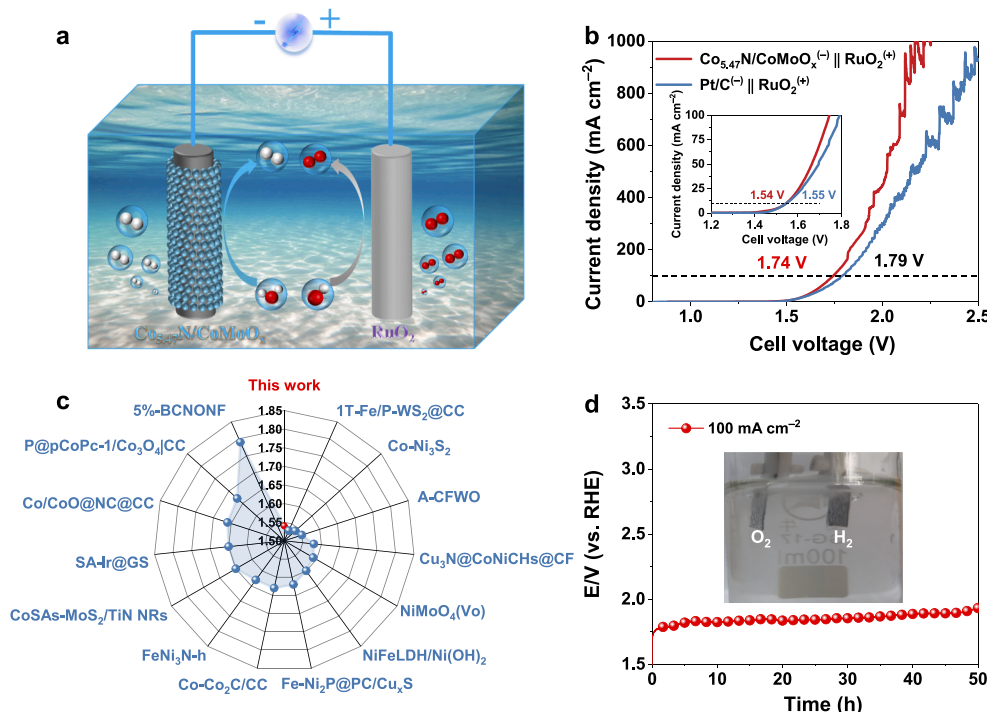
Fig. 6. (a) Schematic diagram of overall water splitting in two-electrode system, (b) polarization curves of $Co_{5.47}N/CoMoO_x^{(-)} \parallel RuO_2^{(+)}$ and $Pt/C^{(-)} \parallel RuO_2^{(+)}$ for overall water splitting in 1.0 M KOH, (c) comparison the cell voltage at 10 mA cm^{-2} with previously reported catalysts in 1.0 M KOH. (d) Chronopotentiometry curve of $Co_{5.47}N/CoMoO_x^{(-)} \parallel RuO_2^{(+)}$ at 100 mA cm^{-2} in 1.0 M KOH.

a two-electrode system of $Co_{5.47}N/CoMoO_x^{(-)} \parallel RuO_2^{(+)}$ was assembled using $Co_{5.47}N/CoMoO_x$ and RuO_2 as the respective cathode and anode to appraise the feasibility for overall water splitting (Fig. 6a). In Fig. 6b, the $Co_{5.47}N/CoMoO_x^{(-)} \parallel RuO_2^{(+)}$ system operated cell voltages of 1.54 and 1.74 V to reach current densities of 10 and 100 mA cm^{-2}, respectively, superior to $Pt/C^{(-)} \parallel RuO_2^{(+)}$. In addition, the overall water splitting performance of $Co_{5.47}N/CoMoO_x$ was preferable to most of the recently reported electrocatalysts (Fig. 6c and Table S5). As illustrated in Fig. 6d, $Co_{5.47}N/CoMoO_x^{(-)} \parallel RuO_2^{(+)}$ could stably operate for 50 h at 100 mA cm^{-2} with negligible performance degradation, implying that it was an efficient and durable electrocatalyst.

The excellent HER performance of $Co_{5.47}N/CoMoO_x$ is due to the following reasons: (1) The self-supporting binder-free electrodes, synthesized in-situ, reduce resistance and improve charge transfer, promoting reaction kinetics. (2) The uniform particle structure enhances the exposure of active sites, promoting electrolyte transport and gas emission. (3) The presence of oxygen vacancies improves conductivity, facilitating charge transfer. (4) The strong synergy between $Co_{5.47}N$, CoO, and $CoMoO_4$, and abundant oxygen vacancies, promote water dissociation and optimize hydrogen adsorption energy, thus enhancing HER performance and kinetics.

4. Conclusions

In summary, the $Co_{5.47}N/CoMoO_x$ hybrid catalyst was investigated experimentally and theoretically. The results indicated that the hybrid catalyst exhibited unusual hydrogen evolution performance in alkaline media. The outstanding performance was attributed to the intense electron interaction and abundant oxygen vacancies in the catalyst, which reduce the water-dissociation energy and accelerate the HER process. Mo^{4+} and Mo^{5+} ions also contribute to the improved HER performance. The $Co_{5.47}N/CoMoO_x$ catalyst showed a low overpotential of 36 mV at 10 mA cm^{-2}, high exchange current density of 3.75 mA cm^{-2}, small charge transfer resistance of 2.1 Ω, and large

electrochemically active surface area of 1775.0 cm^2. The cell voltage of the $Co_{5.47}N/CoMoO_x$-based electrolyzer was lower than that of the commercial Pt/C-based electrolyzer at 100 mA cm^{-2}, indicating a better potential for commercial applications. The uniform particle morphology of the $Co_{5.47}N/CoMoO_x$ hybrid on carbon cloth with rich oxygen vacancies further enhances its performance by providing a large surface area, more active sites, and improving electrolyte transport and gas emission. Our study suggests that interface engineering and defects strategy can be practical approaches for developing high-performance HER catalysts.

CRediT authorship contribution statement

Zhiyang Huang: Writing – original draft. **Zhengqi Liu:** Data curation, Conceptualization. **Miao Liao:** Investigation. **Lixia Wang:** Investigation, Methodology. **Zuyang Luo:** Data curation, Methodology. **Tayirjan Taylor Isimjan:** Writing – review & editing. **Xiulin Yang:** Supervision, Writing – review & editing.

Declaration of Competing Interest

The authors declare that they have no known competing financial interests or personal relationships that could have appeared to influence the work reported in this paper.

Data availability

The data that has been used is confidential.

Acknowledgements

Talents of Guangxi (F-KA18015), and Guangxi Technology Base and Talent Subject (GUIKE AD18126001, GUIKE AD20297039).

Appendix A. Supplementary data

Supplementary data to this article can be found online at https://doi.org/10.1016/j.cej.2023.142281.

References

[1] Q. Yu, Z. Zhang, S. Qiu, Y. Luo, Z. Liu, F. Yang, H. Liu, S. Ge, X. Zou, B. Ding, W. Ren, H.-M. Cheng, C. Sun, B. Liu, A Ta-TaS₂ monolith catalyst with robust and metallic interface for superior hydrogen evolution, Nat. Commun. 12 (2021) 6051, https://doi.org/10.1038/s41467-021-26315-7.

[2] G. Li, H. Jang, S. Liu, Z. Li, M.G. Kim, Q. Qin, X. Liu, J. Cho, The synergistic effect of Hf-O-Ru bonds and oxygen vacancies in Ru/HfO₂ for enhanced hydrogen evolution, Nat. Commun. 13 (2022) 1270, https://doi.org/10.1038/s41467-022-28947-9.

[3] M. Li, Y. Qian, J. Du, H. Wu, L. Zhang, G. Li, K. Li, W. Wang, D.J. Kang, CuS Nanosheets Decorated with CoS₂ Nanoparticles as an Efficient Electrocatalyst for Enhanced Hydrogen Evolution at All pH Values, ACS Sustain. Chem. Eng. 7 (2019) 14016–14022, https://doi.org/10.1021/acssuschemeng.9b02519.

[4] Y. Gao, Z. Chen, Y. Zhao, W. Yu, X. Jiang, M. He, Z. Li, T. Ma, Z. Wu, L. Wang, Facile synthesis of MoP-Ru₂P on porous N, P co-doped carbon for efficiently electrocatalytic hydrogen evolution reaction in full pH range, Appl. Catal. B: Environ. 303 (2022), 120879, https://doi.org/10.1016/j.apcatb.2021.120879.

[5] J. Zhang, T. Wang, D. Pohl, B. Rellinghaus, R. Dong, S. Liu, X. Zhuang, X. Feng, Interface Engineering of MoS₂/Ni₃S₂ Heterostructures for Highly Enhanced Electrochemical Overall-Water-Splitting Activity, Angew. Chem. Int. Ed. 55 (2016) 6702–6707, https://doi.org/10.1002/anie.201602237.

[6] H. Wang, M. Cui, G. Fu, J. Zhang, X. Ding, I. Azaceta, M. Bugnet, D. M. Kepaptsoglou, V.K. Lazarov, V.A. de la Peña O'Shea, F.E. Oropeza, K.H. L. Zhang, Vertically aligned Ni/NiO nanocomposites with abundant oxygen deficient hetero-interfaces for enhanced overall water splitting, Sci. China Chem. 65 (2022) 1885–1894, https://doi.org/10.1007/s11426-022-1326-2.

[7] Y. Shi, D. Zhang, H. Miao, X. Wu, Z. Wang, T. Zhan, J. Lai, L. Wang, Amorphous/2H-MoS₂ nanoflowers with P doping and S vacancies to achieve efficient pH-universal hydrogen evolution at high current density, Sci. China Chem. 65 (2022) 1829–1837, https://doi.org/10.1007/s11426-022-1326-2.

[8] L. Huang, D. Chen, G. Luo, Y.-R. Lu, C. Chen, Y. Zou, C.-L. Dong, Y. Li, S. Wang, Zirconium-Regulation-Induced Bifunctionality in 3D Cobalt-Iron Oxide Nanosheets for Overall Water Splitting, Adv. Mater. 31 (2019) 1901439, https://doi.org/10.1002/adma.201901439.

[9] S. Ma, X. Qu, J. Huang, C. Zhang, G. Chen, W. Chen, T. Li, T. Shao, K. Zheng, J. Tian, C. Li, K. Ostrikov, Compositional and crystallographic design of Ni-Co phosphide heterointerfaced nanowires for high-rate, stable hydrogen generation at industry-relevant electrolysis current densities, Nano Energy 95 (2022), 106989, https://doi.org/10.1016/j.nanoen.2022.106989.

[10] X. Yuan, W. Huang, L. Kong, S. Guo, Y. Cheng, Ditungsten carbide nanoparticles homogeneously embedded in carbon nanofibers for efficient hydrogen production, Chem. Eng. J. 420 (2021) 130480, https://doi.org/10.1016/j.cej.2021.130480.

[11] S.H. Park, T.H. Jo, M.H. Lee, K. Kawashima, C.B. Mullins, H.-K. Lim, D.H. Youn, Highly active and stable nickel–molybdenum nitride (Ni₂Mo₃N) electrocatalyst for hydrogen evolution, J. Mater. Chem. A 9 (2021) 4945–4951, https://doi.org/10.1039/D0TA10090K.

[12] Y. Hu, Z. Luo, M. Guo, J. Dong, P. Yan, C. Hu, T.T. Isimjan, X. Yang, Interface engineering of Co₂N₀.₆₇/CoMoO₄ heterostructure nanosheets as a highly active electrocatalyst for overall water splitting and Zn-H₂O cell, Chem. Eng. J. 435 (2022), 134795, https://doi.org/10.1016/j.cej.2022.134795.

[13] N. Yao, R. Meng, F. Wu, Z. Fan, G. Cheng, W. Luo, Oxygen-Vacancy-Induced CeO₂/Co₄N heterostructures toward enhanced pH-Universal hydrogen evolution reactions, Appl. Catal. B: Environ. 277 (2020), 119282, https://doi.org/10.1016/j.apcatb.2020.119282.

[14] Y. Liu, Y. Xing, S. Xu, Y. Lu, S. Sun, D. Jiang, Interfacing Co₃Mo with CoMoOₓ for synergistically boosting electrocatalytic hydrogen and oxygen evolution reactions, Chem. Eng. J. 431 (2022), 133240, https://doi.org/10.1016/j.cej.2021.133240.

[15] W. Hu, Q. Shi, Z. Chen, H. Yin, H. Zhong, P. Wang, Co₂N/Co₂Mo₃O₈ Heterostructure as a Highly Active Electrocatalyst for an Alkaline Hydrogen Evolution Reaction, ACS Appl. Mater. Interfaces 13 (2021) 8337–8343, https://doi.org/10.1021/acsami.0c20271.

[16] N. Yao, Z. Fan, Z. Xia, F. Wu, P. Zhao, G. Cheng, W. Luo, Constructing the CoO/Co₄N heterostructure with an optimized electronic structure to boost alkaline hydrogen evolution electrocatalysis, J. Mater. Chem. A 9 (2021) 18208–18212, https://doi.org/10.1039/D1TA04691H.

[17] X.H. Chen, X.L. Li, L.L. Wu, H.C. Fu, J. Luo, L. Shen, Q. Zhang, J.L. Lei, H.Q. Luo, N. B. Li, Nb₂O₅–Ni₃N heterojunction tuned by interface oxygen vacancy engineering for the enhancement of electrocatalytic hydrogen evolution activity, J. Mater. Chem. A 9 (2021) 11563–11570, https://doi.org/10.1039/D1TA01872H.

[18] H. Yu, L. Qi, Y. Hu, Y. Qu, P. Yan, T.T. Isimjan, X. Yang, Nanowire-structured FeP-CoP arrays as highly active and stable bifunctional electrocatalyst synergistically promoting high-current overall water splitting, J. Colloid Interface Sci. 600 (2021) 811–819, https://doi.org/10.1016/j.jcis.2021.05.074.

[19] Y.L. Wu, W. Guo, X.J. Lian, Y.M. Tian, W.G. Wang, J.Y. Li, S. Wang, Self-assembled three-dimensional hierarchical CoMoO₄ nanosheets on NiCo₂O₄ for high-performance supercapacitor, J. Alloys Compd. 793 (2019) 418–424, https://doi.org/10.1016/j.jallcom.2019.04.189.

[20] H.C. Fu, X.H. Wang, X.H. Chen, Q. Zhang, N.B. Li, H.Q. Luo, Interfacial engineering of Ni(OH)₂ on W₂C for remarkable alkaline hydrogen production, Appl. Catal. B: Environ. 301 (2021), 120818, https://doi.org/10.1016/j.apcatb.2021.120818.

[21] G. Zhou, G. Liu, X. Liu, Q. Yu, H. Mao, Z. Xiao, L. Wang, 1D/3D Heterogeneous Assembling Body as Trifunctional Electrocatalysts Enabling Zinc-Air Battery and Self-Powered Overall Water Splitting, Adv. Funct. Mater. 32 (2021) 2107608, https://doi.org/10.1002/adfm.202107608.

[22] X. Liu, Z. Yang, L. Zhang, In-situ fabrication of 3D hierarchical flower-like β-Bi₂O₃@CoO Z-scheme heterojunction for visible-driven simultaneous degradation of multi-pollutants, J. Hazard. Mater. 403 (2021), 123566, https://doi.org/10.1016/j.jhazmat.2020.123566.

[23] X. Huang, J. Li, W. Zhang, W. Huang, L. Yang, Q. Gao, Phase Engineering of CoMoO₄ Anode Materials toward Improved Cycle Life for Li⁺ Storage†, Chin. J. Chem. 39 (2021) 1121–1128, https://doi.org/10.1002/cjoc.202000646.

[24] X. Wang, X. Zhang, G. Li, Y. Liu, B. Chen, The influence of facile pre-reaction on the morphology and electrochemical performance of MnO(OH)/Co(OH)₂ composite for supercapacitor, Ionics 26 (2020) 2071–2079, https://doi.org/10.1007/s11581-019-03366-x.

[25] Y. Huang, S.L. Zhang, X.F. Lu, Z.-P. Wu, D. Luan, X.W. Lou, Trimetallic Spinel NiCo₂₋ₓFeₓO₄ Nanoboxes for Highly Efficient Electrocatalytic Oxygen Evolution, Angew. Chem. Int. Ed. 60 (2021) 11841–11846, https://doi.org/10.1002/anie.202103058.

[26] T. Wu, S. Sun, J. Song, S. Xi, Y. Du, B. Chen, W.A. Sasangka, H. Liao, C.L. Gan, G. G. Scherer, L. Zeng, H. Wang, H. Li, A. Grimaud, Z.J. Xu, Iron-facilitated dynamic active-site generation on spinel CoAl₂O₄ with self-termination of surface reconstruction for water oxidation, Nat. Catal. 2 (2019) 763–772, https://doi.org/10.1038/s41929-019-0325-4.

[27] H. Jia, A. Du, H. Zhang, J. Yang, R. Jiang, J. Wang, C.-Y. Zhang, Site-Selective Growth of Crystalline Ceria with Oxygen Vacancies on Gold Nanocrystals for Near-Infrared Nitrogen Photofixation, J. Am. Chem. Soc. 141 (2019) 5083–5086, https://doi.org/10.1021/jacs.8b13062.

[28] Y. Zhang, P. Chen, X. Wang, Q. Wang, K. Zhu, K. Ye, G. Wang, D. Cao, J. Yan, Q. Zhang, High-Capacity and Kinetically Accelerated Lithium Storage in MoO₃ Enabled by Oxygen Vacancies and Heterostructure, Adv. Energy Mater. 11 (2021) 2101712, https://doi.org/10.1002/aenm.202101712.

[29] Z. Li, Q. Jiao, S.-A. He, G. He, Z. Cen, F. Yang, R. Zou, K. Xu, Engineering oxygen vacancies and surface chemical reconstruction of MOF-derived hierarchical CoO/Ni₂-Co₂P nanosheet arrays for advanced aqueous zinc-ion batteries, Dalton Trans. 50 (2021) 17538–17548, https://doi.org/10.1039/D1DT03193G.

[30] B. Wang, M. Zhang, X. Cui, Z. Wang, M. Rager, Y. Yang, Z. Zou, Z.L. Wang, Z. Lin, Unconventional Route to Oxygen-Vacancy-Enabled Highly Efficient Electron Extraction and Transport in Perovskite Solar Cells, Angew. Chem. Int. Ed. 59 (2020) 1611–1618, https://doi.org/10.1002/anie.201910471.

[31] M. Guo, M. Xu, Y. Qu, C. Hu, P. Yan, T.T. Isimjan, X. Yang, Electronic/mass transport increased hollow porous Cu₃P/MoP nanospheres with strong electronic interaction for promoting oxygen reduction in Zn-air batteries, Appl. Catal. B: Environ. 297 (2021), 120415, https://doi.org/10.1016/j.apcatb.2021.120415.

[32] W. Xie, J. Huang, L. Huang, S. Geng, S. Song, P. Tsiakaras, Y. Wang, Novel fluorine-doped cobalt molybdate nanosheets with enriched oxygen-vacancies for improved oxygen evolution reaction activity, Appl. Catal. B: Environ. 303 (2022), 120871, https://doi.org/10.1016/j.apcatb.2021.120871.

[33] Q. Peng, Q. He, Y. Hu, T.T. Isimjan, R. Hou, X. Yang, Interface engineering of porous Fe₂P-WO₂.₉₂ catalyst with oxygen vacancies for highly active and stable large-current oxygen evolution and overall water splitting, J. Energy Chem. 65 (2022) 574–582, https://doi.org/10.1016/j.jechem.2021.06.037.

[34] Y. Hu, H. Yu, L. Qi, J. Dong, P. Yan, T. Taylor Isimjan, X. Yang, Interface Engineering of Needle-Like P-Doped MoS₂/CoP Arrays as Highly Active and Durable Bifunctional Electrocatalyst for Overall Water Splitting, ChemSusChem 14 (2021) 1565–1573, https://doi.org/10.1002/cssc.202002873.

[35] Y. Lu, Z. Li, Y. Xu, L. Tang, S. Xu, D. Li, J. Zhu, D. Jiang, Bimetallic Co-Mo nitride nanosheet arrays as high-performance bifunctional electrocatalysts for overall water splitting, Chem. Eng. J. 411 (2021) 128433, https://doi.org/10.1016/j.cej.2021.128433.

[36] Y.-Z. Li, T.-T. Li, W. Chen, Y.-Y. Song, Co₄N Nanowires: Noble-Metal-Free Peroxidase Mimetic with Excellent Salt- and Temperature-Resistant Abilities, ACS Appl. Mater. Interfaces 9 (2017) 29881–29888, https://doi.org/10.1021/acsami.7b09861.

[37] L. Zhai, X. She, L. Zhuang, Y. Li, R. Ding, X. Guo, Y. Zhang, Y. Zhu, K. Xu, H.J. Fan, S.P. Lau, Modulating Built-In Electric Field via Variable Oxygen Affinity for Robust Hydrogen Evolution Reaction in Neutral Media, Angew. Chem. Int. Ed. 61 (2022), e202116057, https://doi.org/10.1002/anie.202116057.

[38] H. Cheng, T. Kamegawa, K. Mori, H. Yamashita, Surfactant-Free Nonaqueous Synthesis of Plasmonic Molybdenum Oxide Nanosheets with Enhanced Catalytic Activity for Hydrogen Generation from Ammonia Borane under Visible Light, Angew. Chem. Int. Ed. 53 (2014) 2910–2914, https://doi.org/10.1002/anie.201309759.

[39] Y. Chen, J. Yu, J. Jia, F. Liu, Y. Zhang, G. Xiong, R. Zhang, R. Yang, D. Sun, H. Liu, W. Zhou, Metallic Ni₃Mo₃N Porous Microrods with Abundant Catalytic Sites as Efficient Electrocatalyst for Large Current Density and Superstability of Hydrogen Evolution Reaction and Water Splitting, Appl. Catal. B: Environ. 272 (2020), 118956, https://doi.org/10.1016/j.apcatb.2020.118956.

[40] D. Chen, R. Lu, R. Yu, Y. Dai, H. Zhao, D. Wu, P. Wang, J. Zhu, Z. Pu, L. Chen, J. Yu, S. Mu, Work-function-induced Interfacial Built-in Electric Fields in Os-OsSe$_2$ Heterostructures for Active Acidic and Alkaline Hydrogen Evolution, Angew. Chem. Int. Ed. 61 (2022), e202208642, https://doi.org/10.1002/anie.202208642.

[41] Q. Qian, J. Zhang, J. Li, Y. Li, X. Jin, Y. Zhu, Y. Liu, Z. Li, A. El-Harairy, C. Xiao, G. Zhang, Y. Xie, Artificial Heterointerfaces Achieve Delicate Reaction Kinetics towards Hydrogen Evolution and Hydrazine Oxidation Catalysis, Angew. Chem. Int. Ed. 60 (2021) 5984–5993, https://doi.org/10.1002/anie.202014362.

[42] Y. Yang, R. Zeng, Y. Xiong, F.J. DiSalvo, H.D. Abruña, Cobalt-Based Nitride-Core Oxide-Shell Oxygen Reduction Electrocatalysts, J. Am. Chem. Soc. 141 (2019) 19241–19245, https://doi.org/10.1021/jacs.9b10809.

[43] Y. Hu, M. Guo, C. Hu, J. Dong, P. Yan, T. Taylor Isimjan, X. Yang, Engineering cobalt nitride nanosheet arrays with rich nitrogen defects as a bifunctional robust oxygen electrocatalyst in rechargeable Zn–air batteries, J. Colloid Interface Sci. 608 (2022) 2066–2074, https://doi.org/10.1016/j.jcis.2021.10.128.

[44] K. Shah, R. Dai, M. Mateen, Z. Hassan, Z. Zhuang, C. Liu, M. Israr, W.-C. Cheong, B. Hu, R. Tu, C. Zhang, X. Chen, Q. Peng, C. Chen, Y. Li, Cobalt Single Atom Incorporated in Ruthenium Oxide Sphere: A Robust Bifunctional Electrocatalyst for HER and OER, Angew. Chem. Int. Ed. 61 (2021), e202114951, https://doi.org/10.1002/anie.202114951.

[45] Z. Li, Y. Zhang, Y. Feng, C.-Q. Cheng, K.-W. Qiu, C.-K. Dong, H. Liu, X.-W. Du, Co$_3$O$_4$ Nanoparticles with Ultrasmall Size and Abundant Oxygen Vacancies for Boosting Oxygen Involved Reactions, Adv. Funct. Mater. 29 (2019) 1903444, https://doi.org/10.1002/adfm.201903444.

[46] Y. Wang, T. Zhou, K. Jiang, P. Da, Z. Peng, J. Tang, B. Kong, W.-B. Cai, Z. Yang, G. Zheng, Reduced Mesoporous Co$_3$O$_4$ Nanowires as Efficient Water Oxidation Electrocatalysts and Supercapacitor Electrodes, Adv. Energy Mater. 4 (2014) 1400696, https://doi.org/10.1002/aenm.201400696.

[47] Y. Yao, Y. Zhu, C. Pan, C. Wang, S. Hu, W. Xiao, X. Chi, Y. Fang, J. Yang, H. Deng, S. Xiao, J. Li, Z. Luo, Y. Guo, Interfacial sp C-O–Mo Hybridization Originated High-Current Density Hydrogen Evolution, J. Am. Chem. Soc. 143 (2021) 8720–8730, https://doi.org/10.1021/jacs.1c02831.

[48] X. Gao, H. Zhang, Q. Li, X. Yu, Z. Hong, X. Zhang, C. Liang, Z. Lin, Hierarchical NiCo$_2$O$_4$ Hollow Microcuboids as Bifunctional Electrocatalysts for Overall Water-Splitting, Angew. Chem. Int. Ed. 55 (2016) 6290–6294, https://doi.org/10.1002/anie.201600525.

[49] J. Wu, R. Zhao, H. Xiang, C. Yang, W. Zhong, C. Zhang, Q. Zhang, X. Li, N. Yang, Exposing highly active (100) facet on a SnS$_2$/SnO$_2$ electrocatalyst to boost efficient hydrogen evolution, Appl. Catal. B: Environ. 292 (2021), 120200, https://doi.org/10.1016/j.apcatb.2021.120200.

[50] Y. Yang, Q. Dai, L. Shi, Y. Liu, T.T. Isimjan, X. Yang, Electronic Modulation of Pt Nanoparticles on Ni$_3$N–Mo$_2$C by Support-Induced Strategy for Accelerating Hydrogen Oxidation and Evolution, J. Phys. Chem. Lett. 13 (2022) 2107–2116, https://doi.org/10.1021/acs.jpclett.2c00021.

[51] L. Wang, Y. Zhao, Z. Huang, X. Rao, M. Guo, T.T. Isimjan, X. Yang, Interfacial Regulation of Electron-enhanced Co$_2$P−CuP$_2$ Sheet-like Heterostructure as a Robust Bifunctional Electrocatalyst for Overall Water Splitting and Zn−H$_2$O Cell, ChemCatChem 14 (2022), e202101933, https://doi.org/10.1002/cctc.202101933.

[52] B. Zhang, Z. Jiang, X. Shang, S. Li, Z.-J. Jiang, Accelerated hydrogen evolution reaction in Ni$_3$P/MoP$_2$/MoO$_2$ tri-phase composites with rich crystalline interfaces and oxygen vacancies achieved by plasma assisted phosphorization, J. Mater. Chem. A 9 (2021) 25934–25943, https://doi.org/10.1039/D1TA08457G.

[53] Q. Luo, Y. Zhao, L. Sun, C. Wang, H. Xin, J. Song, D. Li, F. Ma, Interface oxygen vacancy enhanced alkaline hydrogen evolution activity of cobalt-iron phosphide/CeO$_2$ hollow nanorods, Chem. Eng. J. 437 (2022) 135376, https://doi.org/10.1016/j.cej.2022.135376.

[54] C. Pi, X. Li, X. Zhang, H. Song, Y. Zheng, B. Gao, A. Kızılaslan, P.K. Chu, K. Huo, In-Plane Mott-Schottky Effects Enabling Efficient Hydrogen Evolution from Mo$_5$N$_6$-MoS$_2$ Heterojunction Nanosheets in Universal-pH Electrolytes, Small 18 (2022) 2201137, https://doi.org/10.1002/smll.202201137.

[55] H. Ma, Z. Chen, Z. Wang, C.V. Singh, Q. Jiang, Interface Engineering of Co/CoMoN/NF Heterostructures for High-Performance Electrochemical Overall Water Splitting, Adv. Sci. 9 (2022), e2105313, https://doi.org/10.1002/advs.202105313.

[56] Q. He, Y. Zhou, H. Shou, X. Wang, P. Zhang, W. Xu, S. Qiao, C. Wu, H. Liu, D. Liu, S. Chen, R. Long, Z. Qi, X. Wu, L. Song, Synergic Reaction Kinetics over Adjacent Ruthenium Sites for Superb Hydrogen Generation in Alkaline Media, Adv. Mater. 34 (2022) 2110604, https://doi.org/10.1002/adma.202110604.

[57] S. Zhou, H. Jang, Q. Qin, L. Hou, M.G. Kim, S. Liu, X. Liu, J. Cho, Boosting Hydrogen Evolution Reaction by Phase Engineering and Phosphorus Doping on Ru/P-TiO$_2$, Angew. Chem. Int. Ed. 61 (2022), e202212196, https://doi.org/10.1002/anie.202212196.

[58] R. Subbaraman, D. Tripkovic, D. Strmcnik, K.-C. Chang, M. Uchimura, P. Paulikas Arvydas, V. Stamenkovic, M. Markovic Nenad, Enhancing Hydrogen Evolution Activity in Water Splitting by Tailoring Li$^+$-Ni(OH)$_2$-Pt Interfaces, Science 334 (2011) 1256–1260, https://doi.org/10.1126/science.1211934.

[59] S. Wen, T. Yang, N. Zhao, L. Ma, E. Liu, Ni-Co-Mo-O nanosheets decorated with NiCo nanoparticles as advanced electrocatalysts for highly efficient hydrogen evolution, Appl. Catal. B Environ. 258 (2019), 117953, https://doi.org/10.1016/j.apcatb.2019.117953.